

# Synthesizing Virtual Oscillators to Control Islanded Inverters

Brian B. Johnson, *Member, IEEE*, Mohit Sinha, Nathan G. Ainsworth, *Member, IEEE*, Florian Dörfler, *Member, IEEE*, and Sairaj V. Dhople, *Member, IEEE*

**Abstract**—Virtual oscillator control (VOC) is a decentralized control strategy for islanded microgrids where inverters are regulated to emulate the dynamics of weakly nonlinear oscillators. Compared to droop control, which is only well defined in sinusoidal steady state, VOC is a time-domain controller that enables interconnected inverters to stabilize arbitrary initial conditions to a synchronized sinusoidal limit cycle. However, the nonlinear oscillators that are elemental to VOC cannot be designed with conventional linear-control design methods. We address this challenge by applying averaging- and perturbation-based nonlinear analysis methods to extract the sinusoidal steady-state and harmonic behavior of such oscillators. The averaged models reveal conclusive links between real- and reactive-power outputs and the terminal-voltage dynamics. Similarly, the perturbation methods aid in quantifying higher order harmonics. The resultant models are then leveraged to formulate a design procedure for VOC such that the inverter satisfies standard ac performance specifications related to voltage regulation, frequency regulation, dynamic response, and harmonic content. Experimental results for a single-phase 750 VA, 120 V laboratory prototype demonstrate the validity of the design approach. They also demonstrate that droop laws are, in fact, embedded within the equilibria of the nonlinear-oscillator dynamics. This establishes the backward compatibility of VOC in that, while acting on time-domain waveforms, it subsumes droop control in sinusoidal steady state.

**Index Terms**—Averaging, droop control, microgrids, nonlinear oscillator circuits, synchronization, Van der Pol oscillators.

## I. INTRODUCTION

**M**ICROGRIDS are a collection of heterogeneous energy sources, e.g., photovoltaic arrays, fuel cells, and energy

storage devices, interfaced to an ac electric distribution network that can be islanded and operated independently from the bulk ac system. Energy conversion is often performed by power electronic inverters, and in islanded settings, the control challenge is to regulate the amplitude and frequency of the inverters' terminal voltage such that the high power quality can be guaranteed to the loads in the network. The ubiquitous control strategy in this domain is droop control, which linearly trades off the inverter-voltage amplitude and frequency with real- and reactive-power output [1]. Departing from droop control, in the spirit of pioneering time-domain control methods first proposed in [2] and [3], and building further on our prior work [4], we focus on a nonlinear control strategy where islanded inverters are controlled to emulate the dynamics of weakly nonlinear limit-cycle oscillators. We have termed this strategy *virtual oscillator control* (VOC) since the nonlinear oscillators are programmed on a digital controller. VOC presents appealing circuit- (inverter) and system- (microgrid electrical network) level advantages. From a system-level perspective, synchronization emerges in connected electrical networks of inverters with VOC without any communication, and primary-level voltage- and frequency-regulation objectives are ensured in a decentralized fashion [5]. At the circuit level, each inverter is able to rapidly stabilize arbitrary initial conditions and load transients to a stable limit cycle. As such, VOC is fundamentally different compared to droop control. While VOC acts on instantaneous time-domain signals, droop control is based on phasorial electrical quantities and the notion of an electrical frequency that are only well defined on slow ac-cycle time scales. It, however, emerges that the sinusoidal state behavior of VOC can be engineered to correspond to droop laws [5]. (We comment further on this aspect shortly.)

This paper focuses on the design of virtual oscillators that underpin the control strategy; we refer to this as the *oscillator synthesis problem*. Inverter ac performance requirements (voltage and frequency regulation, harmonics, dynamic response) are typically specified with the aid of phasor quantities that are only valid in the quasi-stationary sinusoidal steady state. As such, given the intractability of obtaining closed-form solutions to the oscillator dynamic trajectories, from the outset it is unclear how to design the nonlinear oscillators such that the controlled inverters meet prescribed specifications. We address the oscillator synthesis problem with averaging- and perturbation-based nonlinear-systems analysis methods [6]–[8]. Leveraging our previous work in [5], we focus on an averaged dynamical model for the nonlinear oscillators that couples the real- and reactive-power outputs to the terminal-voltage dynamics of the inverter. Analyzing this averaged model in the sinusoidal steady

Manuscript received January 31, 2015; revised May 16, 2015, August 8, 2015, and September 13, 2015; accepted October 16, 2015. Date of publication November 3, 2015; date of current version March 2, 2016. The work of B. B. Johnson and N. G. Ainsworth was supported by the Laboratory Directed Research and Development program at NREL and by the U.S. Department of Energy under Contract DE-AC36-08-GO28308 with NREL. The work of M. Sinha and S. V. Dhople was supported in part by the National Science Foundation under the CAREER Award, ECCS-CAR-1453921, Grant ECCS-1509277, and by the Office of Naval Research under Grant N000141410639. The work of F. Dörfler was supported by ETH Zürich funds and the SNF Assistant Professor Energy Grant #160573. Recommended for publication by Associate Editor Y. Sozer.

B. B. Johnson and N. G. Ainsworth are with the Power Systems Engineering Center at the National Renewable Energy Laboratory, Golden, CO 80401 USA (e-mail: brian.johnson@nrel.gov; nathan.ainsworth@nrel.gov).

M. Sinha and S. V. Dhople are with the Department of Electrical and Computer Engineering, University of Minnesota, Minneapolis, MN 55414 USA (e-mail: sinha052@umn.edu; sdhople@umn.edu).

F. Dörfler is with the Automatic Control Laboratory at ETH Zürich, Zürich 8092, Switzerland (e-mail: dorfler@ethz.ch).

Color versions of one or more of the figures in this paper are available online at <http://ieeexplore.ieee.org>.

Digital Object Identifier 10.1109/TPEL.2015.2497217

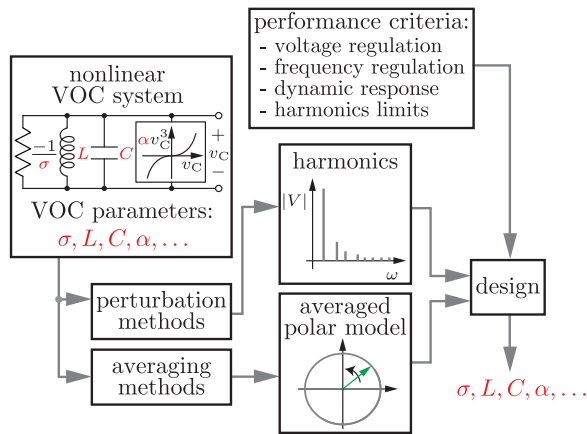


Fig. 1. Nonlinear-systems analysis methods enable the formulation of a design strategy that relates inverter performance criteria to the oscillator circuit parameters (indicated in red).

state uncovers the voltage- and frequency-regulation characteristics of virtual-oscillator-controlled (VO-controlled) inverters. In addition, we develop perturbation-based methods that, in general, enable approximating solutions to periodic nonlinear dynamical systems when analytical closed-form solutions cannot be found. In the present setting, this analysis parameterizes the higher order harmonic content in the inverter output as a function of the oscillator parameters, further aiding in oscillator design. The design strategy developed in this paper is summarized and illustrated in Fig. 1.

The contributions of this paper are threefold. First, we present a systematic design strategy to synthesize nonlinear oscillators for inverter control. The design strategy aids in sculpting a desirable sinusoidal limit cycle that meets performance requirements specified in the lexicon of ac power systems. The proposed strategy can be conveniently applied to design controllers for inverters with different power, voltage, and current ratings; in fact, for a system of parallel-connected inverters, the proposed design strategy natively ensures power sharing in proportion to the inverter power ratings. Second, in addition to demonstrating the validity of our design strategy, our experimental results also validate the accuracy of averaging- and perturbation-based nonlinear-systems analysis methods that are ubiquitous in modeling, analysis, and control of weakly nonlinear periodic systems in application areas such as electrical power systems, circadian rhythms, and bipedal walking machines [6], [9]. With regard to power-electronics-based systems, averaging methods at switching-frequency time scales have been successfully applied in prior works to extract analytically tractable models for simulation and controller design [10]–[15]. Finally, our previous work has demonstrated that droop laws are embedded within a slower time scale in the nonlinear dynamics of a family of weakly nonlinear limit-cycle oscillators [5]. In this paper, we provide experimental evidence to substantiate this—rather surprising and bold—claim.

Tangentially related to our work are previous efforts in the design of droop-controlled inverters. Particularly, there exists a wide body of the literature that attempts to identify droop-

control parameters that ensure inverters satisfy steady-state performance metrics and constraints such as voltage regulation, maximum frequency deviation, and proportional power sharing [16]–[20]. For our previous efforts in realizing VOC, we relied on an iterative design procedure involving simulation-based open-circuit and full-rated-load tests to design the virtual oscillators [4], [21], [22]. These ad hoc design methods relied on repeated time-domain simulations to tune parameters and were not affirmed by a rigorous nonlinear-systems analysis approach. Through developing a unified and formal design methodology for VOC, we expect this paper to particularly benefit practicing engineers who would be interested in implementation aspects.

While this paper focuses on inverter-level design, our previous work has analyzed the system-level attributes of VOC. Particularly, in [4], we consider a parallel-connected system of VO-controlled inverters, and provide i) analytical conditions for global asymptotic synchronization, and ii) experimental results that demonstrate power sharing, ability to serve linear and nonlinear loads, robustness to parameter variations, and asymptotic decay of circulating currents. We have also extended our analytical approach to cover arbitrary resistive networks in [5], where we establish the existence of well-defined equilibria of the system dynamics, as well as local exponential stability of linearized amplitude and phase dynamics.

A Van der Pol oscillator constitutes the virtual oscillator in this paper. We remark that the techniques outlined here can be applied to a family of weakly nonlinear limit-cycle oscillators. Subsequently, where we reference VOC, we imply the control strategy is implemented with Van der Pol oscillators [6], [23]; also, inverters controlled with this approach are termed as VO-controlled inverters.

The remainder of this paper is organized as follows. Averaging and perturbation techniques are developed in Section II. A design procedure which accounts for multiple design objectives is described in Section III, and the proposed design framework is experimentally validated in Section IV. Concluding remarks and directions for future work are given in Section V. The reader who is mainly interested in practical application can skip the analysis in Section II and go directly to Sections III and IV where we outline a straightforward design procedure and comment on how the controller could be discretized for digital implementation.

## II. INVERTER TERMINAL-VOLTAGE DYNAMICS: REGULATION, DYNAMIC RESPONSE, AND HARMONICS

In this section, we outline the dynamical model that captures the ac time-scale behavior of the inverter terminal voltage. The model conclusively establishes a link between the inverter terminal-voltage amplitude and frequency with the average real- and reactive-power output. This is leveraged to derive the voltage- and frequency-regulation characteristics of VO-controlled inverters. Furthermore, the averaged model also enables a characterization of the dynamic response of VO-controlled inverters. Finally, we also analyze the higher order harmonics in the voltage waveforms. The models and analyses outlined in this section are leveraged for system design

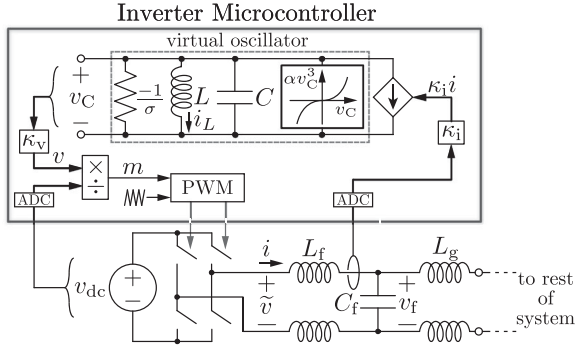


Fig. 2. Implementation of VOC on a single-phase H-bridge inverter with an  $LCL$  output filter. The closed-loop controller is a discrete realization of the nonlinear dynamics of a Van der Pol oscillator programmed on a microcontroller. The current and voltage scalings  $\kappa_v$  and  $\kappa_i$  interface the virtual oscillator to the inverter.

subsequently in Section III. We begin with a brief overview of the controller implementation.

#### A. Controller Implementation

Fig. 2 illustrates the Van der Pol VOC implementation for a single-phase inverter. The hardware also includes an  $LCL$  filter, which is utilized to reduce the high-order harmonics in the inverter terminal voltage. Filter elements include the inverter-side inductor  $L_f$ , the ac filter capacitor  $C_f$ , and the grid-side inductor  $L_g$ . The closed-loop controller is a discretized version of the Van der Pol oscillator dynamics programmed onto a digital microcontroller.

The circuit model of the Van der Pol oscillator is composed of the parallel connection of i) a harmonic oscillator with inductance  $L$  and capacitance  $C$  (yielding a resonant frequency,  $\omega^* = 1/\sqrt{LC}$ ), ii) a negative-conductance element  $-\sigma$ , and iii) a cubic voltage-dependent current source. The virtual capacitor voltage is denoted by  $v_C$  and the inductor current is denoted by  $i_L$ . The current consumed by the cubic voltage-dependent current source is given by  $\alpha v_C^3$ , where  $\alpha$  is a positive constant.

The virtual oscillator is coupled to physical electrical signals in the inverter through the voltage- and current-scaling gains  $\kappa_v$  and  $\kappa_i$ , respectively. The inverter output current  $i$  is processed by an analog-to-digital converter (ADC), multiplied by  $\kappa_i$ , and is extracted from the Van der Pol oscillator circuit. The resulting value of the VO capacitor voltage  $v_C$  is scaled by  $\kappa_v$  to produce the signal  $v$ , and this is used to construct the pulse width modulation (PWM) signal which drives the H-bridge inverter. For the single-phase inverter topology depicted in Fig. 2, the PWM signal  $m(t)$  is constructed as follows:

$$m(t) = \frac{v(t)}{v_{dc}}, \quad (1)$$

where  $v_{dc}$  is the dc bus voltage. The switching period  $T_{sw}$  is much smaller than the period of the modulation signal, which in this setting is approximately  $2\pi/\omega^*$ , where  $\omega^*$  is the resonant frequency of the  $LC$  harmonic oscillator. Consequently,

the switch-cycle average of the instantaneous inverter-terminal voltage—denoted by  $\tilde{v}$  in Fig. 2—is approximately equal to the scaled virtual capacitor voltage  $v$  [24]

$$\frac{1}{T_{sw}} \int_{s=t-T_{sw}}^t \tilde{v}(s) ds = m(t)v_{dc} = v(t). \quad (2)$$

We subsequently assume that the switch-cycle-average inverter terminal voltage is equal to  $v$  and we refer to this as the *inverter terminal voltage*.

With the controller description in place, we next present an analysis of the terminal-voltage dynamics of a VO-controlled inverter. The dynamic model is leveraged to synthesize the underlying Van der Pol oscillator such that the inverter meets ac performance specifications. Without loss of generality, we focus on real- and reactive-power ratings, voltage limits, output-current ratings, maximum frequency deviation, dynamic response, and higher order harmonics. A key challenge is to connect these performance specifications to the inherently nonlinear Van der Pol oscillator dynamics. The modeling approaches to establish these connections are presented next.

#### B. Averaged Dynamics of a VO-controlled Inverter

We begin with a derivation of the voltage- and frequency-regulation characteristics of the VO-controlled inverter. The derivation is based on an averaging analysis of the Van der Pol oscillator dynamics.

The dynamics of the virtual-oscillator inductor current,  $i_L$ , and the inverter terminal voltage,  $v$ , are given by (see Fig. 2)

$$\begin{aligned} L \frac{di_L}{dt} &= \frac{v}{\kappa_v}, \\ C \frac{dv}{dt} &= -\alpha \frac{v^3}{\kappa_v^2} + \sigma v - \kappa_v i_L - \kappa_i i. \end{aligned} \quad (3)$$

The inverter terminal voltage is parameterized in one of the two forms below

$$v(t) = \sqrt{2}V(t) \cos(\omega t + \theta(t)) = \sqrt{2}V(t) \cos(\phi(t)), \quad (4)$$

where  $\omega$  is the electrical frequency,  $\theta(t)$  represents the phase offset with respect to  $\omega$ , and  $\phi(t)$  is the instantaneous phase angle. We are interested in obtaining the dynamical equations that govern the evolution of the RMS voltage  $V(t)$  and phase offset  $\theta(t)$  (or equivalently, the instantaneous phase angle  $\phi(t)$ ); together these would completely specify the terminal voltage at any instant. To this end, we begin with the following definitions that help us to simplify notation subsequently:

$$\varepsilon := \sqrt{\frac{L}{C}}, \quad g(y) := y - \frac{\beta}{3}y^3, \quad \beta := \frac{3\alpha}{\kappa_v^2\sigma}. \quad (5)$$

A state-space model of the VO-controlled inverter in Cartesian coordinates aimed at recovering the RMS-voltage amplitude and instantaneous phase dynamics can be formulated with a scaled version of the inductor current and the inverter terminal voltage selected as states  $x := \kappa_v \varepsilon i_L$ , and  $y := v$ . With the aid of the  $g(\cdot)$  and  $\varepsilon$  defined in (5), (3) can be rewritten in the time

coordinates  $\tau = \omega^* t = (1/\sqrt{LC})t$  as follows:

$$\dot{x} = \frac{dx}{d\tau} = y, \quad (6)$$

$$\dot{y} = \frac{dy}{d\tau} = -x + \varepsilon \sigma g(y) - \varepsilon \kappa_v \kappa_i i. \quad (7)$$

Next, with the coordinate transformation

$$\sqrt{2}V = \sqrt{x^2 + y^2}, \quad \phi = \tan^{-1}\left(\frac{x}{y}\right), \quad (8)$$

applied to (6) and (7), we recover the following dynamical model for the RMS terminal-voltage amplitude  $V$  and the instantaneous phase angle  $\phi$

$$\begin{aligned} \dot{V} &= \frac{dV}{d\tau} = \frac{\varepsilon}{\sqrt{2}} \left( \sigma g(\sqrt{2}V \cos(\phi)) - \kappa_v \kappa_i i \right) \cos(\phi), \\ \dot{\phi} &= \frac{d\phi}{d\tau} = 1 - \frac{\varepsilon}{\sqrt{2}V} \left( \sigma g(\sqrt{2}V \cos(\phi)) - \kappa_v \kappa_i i \right) \sin(\phi). \end{aligned} \quad (9)$$

As  $\varepsilon \searrow 0$ , we transition the so-called *quasi-harmonic limit*, where the (unloaded) oscillator exhibits near-sinusoidal oscillations at the resonant frequency of the  $LC$  harmonic oscillator [23]

$$\omega^* = \frac{1}{\sqrt{LC}}. \quad (10)$$

In subsequent sections of the paper focused on system design, we will demonstrate how  $\varepsilon$  is a key design parameter that has bearing on the dynamic response and the harmonics of the system—in particular, a small value of  $\varepsilon$  ensures near sinusoidal oscillations, at the expense of a sluggish dynamic response.

Since we will be focused on the parametric regime characterized by  $\varepsilon \searrow 0$ , we can leverage notions of periodic averaging to further simplify and analyze the weakly nonlinear periodic dynamics in (9). As a primer, consider a time-varying dynamical system  $\dot{x} = \varepsilon f(x, \tau, \varepsilon)$  with time-periodic vector field

$$f(x, \tau, \varepsilon) = f(x, \tau + T, \varepsilon), \quad (11)$$

with period  $T > 0$  and a small parameter  $\varepsilon > 0$ . We define the associated *time-averaged* dynamical system [7] as

$$\dot{\bar{x}} = \varepsilon f_{\text{avg}}(\bar{x}) = \frac{\varepsilon}{T} \int_{\tau=0}^T f(\bar{x}, \tau, 0) d\tau. \quad (12)$$

The averaged system  $f_{\text{avg}}(\bar{x})$  is autonomous and, in general, more amenable to analysis compared to the original nonaveraged system  $f(x, \tau, \varepsilon)$ . Furthermore, for  $\varepsilon \searrow 0$ , we do not compromise accuracy by analyzing the averaged system, since it follows that the difference in the state variables corresponding to the original and averaged systems is of  $\mathcal{O}(\varepsilon)$  [7] (see also Fig. 3). In particular, we have

$$x(\tau, \varepsilon) - \bar{x}(\varepsilon\tau) = \mathcal{O}(\varepsilon). \quad (13)$$

Subsequently, we will denote the time average of a periodic signal  $x(t)$  with period  $T > 0$  by  $\bar{x}$ , and define it as follows:

$$\bar{x} := \frac{1}{T} \int_{s=0}^T x(s) ds. \quad (14)$$

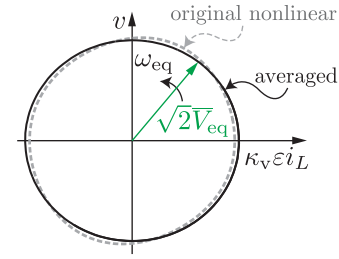


Fig. 3. Superimposed steady-state limit cycles of the original nonlinear oscillator dynamics and the corresponding averaged model. The limit cycle of the averaged model can be described with a circle of fixed radius  $\sqrt{2}\bar{V}_{\text{eq}}$  and constant rotational frequency  $\omega_{\text{eq}}$  in quasi-stationary sinusoidal steady state;  $\bar{V}_{\text{eq}}$  and  $\omega_{\text{eq}}$  depend on the real and reactive power delivered by the oscillator, respectively [see (19) and (23)].

With these preliminaries in place, the dynamics in (9) averaged over one ac cycle  $2\pi/\omega^*$  under the implicit assumption that  $\varepsilon = \sqrt{L/C} \searrow 0$  are given by the following set of coupled nonlinear differential equations:

$$\frac{d}{dt} \bar{V} = \frac{\sigma}{2C} \left( \bar{V} - \frac{\beta}{2} \bar{V}^3 \right) - \frac{\kappa_v \kappa_i}{2C\bar{V}} \bar{P}, \quad (15)$$

$$\frac{d}{dt} \bar{\theta} = \omega^* - \omega + \frac{\kappa_v \kappa_i}{2C\bar{V}^2} \bar{Q}, \quad (16)$$

where  $\bar{P}$  and  $\bar{Q}$  are the average real- and reactive-power outputs of the VO-controlled inverter (measured with respect to the nominal frequency  $\omega^*$ ), respectively. See Appendix A for a brief derivation of (15) and (16), and [5] for more details. Fig. 3 plots limit cycles recovered from i) the original nonlinear dynamics, and ii) the averaged model for a Van der Pol oscillator.

Remarkably, with this nonlinear control strategy, it emerges that close to the sinusoidal steady state (recovered in the quasi-harmonic limit  $\varepsilon \searrow 0$ ), the voltage-amplitude and phase dynamics are directly linked to the average real- and reactive-power outputs of the inverter, respectively. Consequently, these averaged dynamics can be leveraged for synthesizing virtual oscillators so that the inverter satisfies voltage- and frequency-regulation specifications in the sinusoidal steady state. To this end, we will find the equilibrium solutions corresponding to (15) and (16) useful, since they establish the voltage- and frequency-regulation characteristics of the VO-controlled inverter.

1) *Voltage-regulation Characteristic:* The equilibria of (15) can be recovered from the solutions of the nonlinear equation

$$0 = \frac{\sigma}{2C} \left( \bar{V}_{\text{eq}} - \frac{\beta}{2} \bar{V}_{\text{eq}}^3 \right) - \frac{\kappa_v \kappa_i}{2C\bar{V}_{\text{eq}}} \bar{P}_{\text{eq}}, \quad (17)$$

where  $\bar{V}_{\text{eq}}$  and  $\bar{P}_{\text{eq}}$  represent the equilibrium steady-state RMS-voltage amplitude and average real-power output, respectively. Rearranging terms in (17), we get the following power balance condition for the VO-controlled inverter:

$$\frac{\sigma\beta}{2} \bar{V}_{\text{eq}}^4 - \sigma \bar{V}_{\text{eq}}^2 + \kappa_v \kappa_i \bar{P}_{\text{eq}} = 0. \quad (18)$$



The positive roots of (18) are given by

$$\bar{V}_{\text{eq}} = \kappa_v \left( \frac{\sigma \pm \sqrt{\sigma^2 - 6\alpha(\kappa_i/\kappa_v)\bar{P}_{\text{eq}}}}{3\alpha} \right)^{\frac{1}{2}}, \quad (19)$$

where we have used the fact that  $\sigma\beta = 3\alpha/\kappa_v^2$  [see (5)]. Notice that (19) has two roots. Both roots are real valued if the equilibrium real-power output satisfies

$$0 < \bar{P}_{\text{eq}} < \bar{P}_{\text{cr}} := \frac{\sigma^2}{6\alpha(\kappa_i/\kappa_v)}, \quad (20)$$

where  $\bar{P}_{\text{cr}}$  is referred to as the *critical value* for real power. The corresponding critical value of the terminal voltage is given by

$$\bar{V}_{\text{cr}} := \kappa_v \sqrt{\frac{\sigma}{3\alpha}}. \quad (21)$$

Under a set of mild power-flow decoupling approximations, the high-voltage solution in (19) is locally asymptotically stable (see Appendix B for details). Subsequently, we will refer to the high-voltage solution of (19) by  $\bar{V}_{\text{eq}}$  with a slight abuse of notation. It is worth mentioning that the high-voltage root is a decreasing function of  $\bar{P}_{\text{eq}}$  over the range  $0 \leq \bar{P}_{\text{eq}} \leq \bar{P}_{\text{cr}}$  (that is, steady-state voltage “droops” with increasing real power output). Finally, note that the open-circuit voltage of the VO-controlled inverter  $\bar{V}_{\text{oc}}$  can be obtained by substituting  $\bar{P}_{\text{eq}} = 0$  into the high-voltage root in (19)

$$\bar{V}_{\text{oc}} = \kappa_v \sqrt{\frac{2\sigma}{3\alpha}}. \quad (22)$$

**2) Frequency-Regulation Characteristic:** Consider the phasor-angle dynamics in (16). The equilibrium of (16) returns the frequency of the VO-controlled inverter

$$\omega_{\text{eq}} = \omega^* + \frac{\kappa_v \kappa_i}{2C\bar{V}_{\text{eq}}^2} \bar{Q}_{\text{eq}}, \quad (23)$$

where  $\bar{V}_{\text{eq}}$  is the stable high-voltage equilibrium obtained from (19), and  $\bar{Q}_{\text{eq}}$  is the average reactive-power output of the VO-controlled inverter.

### C. Dynamic Response

In this section, we focus on the dynamic response of the VO-controlled inverter. We are interested in how quickly the terminal voltage of an unloaded inverter builds up to the open-circuit voltage. The voltage dynamics of interest are recovered from (15) by setting  $\bar{P} = 0$

$$\frac{d}{dt}\bar{V} = \frac{\sigma}{2C} \left( \bar{V} - \beta \frac{1}{2}\bar{V}^3 \right). \quad (24)$$

Since (24) is a variable-separable ordinary differential equation, we integrate both sides, setting the limits from  $0.1\bar{V}_{\text{oc}}$  to  $0.9\bar{V}_{\text{oc}}$  (without loss of generality). The time taken for this excursion is defined as the *rise time*; it is denoted by  $t_{\text{rise}}$ , and given by the solution of

$$t_{\text{rise}} = \frac{2}{\varepsilon\sigma} \left[ \log \bar{V} - \frac{1}{2} \log \left| 1 - \frac{\beta}{2}\bar{V}^2 \right| \right]_{0.1\bar{V}_{\text{oc}}}^{0.9\bar{V}_{\text{oc}}}.$$

Evaluating the limits above, we recover [5]

$$t_{\text{rise}} \approx \frac{6}{\omega^* \varepsilon \sigma}. \quad (25)$$

The approximation in (25) indicates that the rise time  $t_{\text{rise}}$  is inversely proportional to  $\varepsilon$ . This aspect will be leveraged in the design of the oscillator capacitance  $C$  in Section III-C. (Recall from (5) that  $\varepsilon = \sqrt{L/C}$ .)

Without loss of generality, we present the above analysis for an unloaded inverter. For an inverter loaded to its rated real power rating with a resistive load  $R_{\text{rated}}$ , the rise time is given by  $t_{\text{rise}} \approx \frac{6}{\omega^* \varepsilon \sigma'}$ , where  $\sigma' = \left( \sigma - \frac{\kappa_v \kappa_i}{R_{\text{rated}}} \right)$ . The subsequent analysis on inverter design can be performed with this specification of rise time if need be.

### D. Harmonics Analysis

In this section, we derive a closed-form analytical expression for the amplitude of the third harmonic of an unloaded VO-controlled inverter. In particular, we will investigate the effect of the nonlinear forcing term in (3), as executed within the digital controller, on the low-order harmonic content of the ac output. Our analysis is aimed at parameter selection with the aim of bounding the ratio of the amplitude of the third harmonic to the fundamental. To this end, we rely on *perturbation methods* and the *method of multiple scales* [25] that seek approximate analytical solutions to nonlinear dynamical systems where exact solutions cannot be found.

Consider the nonaveraged dynamics of the terminal-voltage magnitude in an unloaded VO-controlled inverter

$$\ddot{v} - \varepsilon\sigma(1 - \beta v^2)\dot{v} + v = 0, \quad (26)$$

where  $\varepsilon$  and  $\beta$  are defined in (5), and as before, we operate in the quasi-harmonic limit  $\varepsilon \searrow 0$ . This model follows from expressing (6) and (7) as a second-order system with the input current  $i = 0$ . We seek an approximate solution to (26) that can be expressed as

$$v(\tau, \varepsilon) \approx v_0(\tau, \tilde{\tau}) + \varepsilon v_1(\tau, \tilde{\tau}). \quad (27)$$

The solution is written with respect to two time scales: the original time scale  $\tau$ , and a slower time scale  $\tilde{\tau} := \varepsilon\tau$ . While higher order time scales, i.e.,  $\varepsilon^2\tau$ ,  $\varepsilon^3\tau$ , can be analyzed in a similar fashion to obtain the approximate solutions correct to higher order terms, our analysis is i) valid up to  $\mathcal{O}(\varepsilon)$ , ii) yields an approximate amplitude for the third harmonic, and iii) provides error terms of  $\mathcal{O}(\varepsilon^2)$ . Substituting (27) into (26), and retaining only  $\mathcal{O}(\varepsilon)$  terms, we get

$$\begin{aligned} \left( \frac{\partial^2 v_0}{\partial \tau^2} + v_0 \right) + \varepsilon \left( \frac{\partial^2 v_1}{\partial \tau^2} + v_1 + 2 \frac{\partial^2 v_0}{\partial \tau \partial \tilde{\tau}} - \sigma(1 - \beta v_0^2) \frac{\partial v_0}{\partial \tau} \right) \\ = 0. \end{aligned} \quad (28)$$

Note that (28) must hold for any small parameter  $\varepsilon$ ; this can be ensured if

$$\frac{\partial^2 v_0}{\partial \tau^2} + v_0 = 0, \quad (29)$$

$$\frac{\partial^2 v_1}{\partial \tau^2} + v_1 + 2 \frac{\partial^2 v_0}{\partial \tau \partial \tilde{\tau}} - \sigma(1 - \beta v_0^2) \frac{\partial v_0}{\partial \tau} = 0. \quad (30)$$

Since (29) represents the dynamics of a simple harmonic oscillator, the corresponding closed-form solution can be expressed as

$$v_0(\tau, \tilde{\tau}) = a_0(\tilde{\tau}) \cos(\tau + \rho_0(\tilde{\tau})), \quad (31)$$

where  $a_0(\tilde{\tau})$  and  $\rho_0(\tilde{\tau})$  are amplitude and phase terms that vary in the slow time scale specified by  $\tilde{\tau}$ . For notational convenience, define the orthogonal signal  $v_0^\perp(\tau, \tilde{\tau})$  associated with  $v_0(\tau, \tilde{\tau})$  in (31) as follows:

$$v_0^\perp(\tau, \tilde{\tau}) := a_0(\tilde{\tau}) \sin(\tau + \rho_0(\tilde{\tau})). \quad (32)$$

Substituting for  $v_0$  from (31) into (30)

$$\begin{aligned} \frac{\partial^2 v_1}{\partial \tau^2} + v_1 &= -2 \frac{\partial^2 v_0}{\partial \tau \partial \tilde{\tau}} + \sigma(1 - \beta v_0^2) \frac{\partial v_0}{\partial \tau} \\ &= 2 \frac{\partial v_0^\perp}{\partial \tilde{\tau}} - \sigma v_0^\perp + \sigma \beta v_0^2 v_0^\perp \\ &= 2 \frac{\partial a_0}{\partial \tilde{\tau}} \sin(\tau + \rho_0) + 2 v_0 \frac{\partial \rho_0}{\partial \tilde{\tau}} \\ &\quad - \sigma v_0^\perp + \sigma \beta a_0^3 (\sin(\tau + \rho_0) - \sin^3(\tau + \rho_0)) \\ &= 2 \frac{\partial a_0}{\partial \tilde{\tau}} \sin(\tau + \rho_0) + 2 v_0 \frac{\partial \rho_0}{\partial \tilde{\tau}} \\ &\quad - \sigma v_0^\perp + \frac{\sigma \beta}{4} a_0^3 (\sin(3\tau + 3\rho_0) + \sin(\tau + \rho_0)), \end{aligned} \quad (33)$$

where in the last line of (33), we have used the trigonometric identity  $\sin 3\theta = 3 \sin \theta - 4 \sin^3 \theta$ . Grouping together the coefficients that multiply the  $\sin(\tau + \rho_0)$  and  $\cos(\tau + \rho_0)$  terms, we can rewrite the last line of (33) as follows:

$$\begin{aligned} \frac{\partial^2 v_1}{\partial \tau^2} + v_1 &= \left( 2 \frac{\partial a_0}{\partial \tilde{\tau}} - \sigma a_0 + \frac{\sigma \beta}{4} a_0^3 \right) \sin(\tau + \rho_0), \\ &\quad + \left( 2 a_0 \frac{\partial \rho_0}{\partial \tilde{\tau}} \right) \cos(\tau + \rho_0) \\ &\quad + \frac{\sigma \beta}{4} a_0^3 \sin(3\tau + 3\rho_0). \end{aligned} \quad (34)$$

The coefficients that multiply the  $\sin(\tau + \rho_0)$  and  $\cos(\tau + \rho_0)$  terms have to be forced to zero to ensure that unbounded terms of the form  $\tau \sin(\tau + \rho_0)$  and  $\tau \cos(\tau + \rho_0)$  do not appear in

the solution for  $v_1$ .<sup>1</sup> Consequently, we recover the following:

$$2 \frac{\partial a_0(\tilde{\tau})}{\partial \tilde{\tau}} - \sigma a_0(\tilde{\tau}) + \frac{\sigma \beta}{4} a_0(\tilde{\tau})^3 = 0, \quad (35)$$

$$2 a_0(\tilde{\tau}) \frac{\partial \rho_0(\tilde{\tau})}{\partial \tilde{\tau}} = 0. \quad (36)$$

Solving (36) with initial condition  $a_0(0)$ , we get the following expression for  $a_0(\tilde{\tau})$ :

$$a_0(\tilde{\tau}) = \left( \frac{\beta}{4} + e^{-\eta - \sigma \tilde{\tau}} \right)^{-\frac{1}{2}}, \quad e^\eta = \frac{a_0^2(0)}{1 - \frac{\beta}{4} a_0^2(0)}. \quad (37)$$

It follows that the peak amplitude of the first harmonic in sinusoidal steady state is given by

$$\lim_{\tilde{\tau} \rightarrow \infty} a_0(\tilde{\tau}) =: a_0 = \frac{2}{\sqrt{\beta}}. \quad (38)$$

Note that the RMS value corresponding to the peak amplitude in (38) matches the expression for the open-circuit voltage in (22). From (37), it can also be inferred that  $a_0(\tilde{\tau}) \neq 0$  if  $a_0(0) \neq 0$ . Therefore, we see from (35) that  $\rho_0(\tilde{\tau}) = \rho_0$ , i.e.,  $\rho_0$  is independent of  $\tilde{\tau}$ .

With these observations in place, we finally recover the following equation that governs the evolution of  $v_1(\tau, \tilde{\tau})$  from (34)

$$\frac{\partial^2 v_1}{\partial \tau^2} + v_1 = \frac{2\sigma}{\sqrt{\beta}} \sin(3\tau + 3\rho_0). \quad (39)$$

The particular solution to (39) is given by the general form

$$v_1(\tau) = -\frac{\sigma}{4\sqrt{\beta}} \sin(3\tau + 3\rho_0). \quad (40)$$

From (31), (38), (40), and (27), we see that the ratio of the amplitude of the third harmonic to the fundamental, a quantity we denote by  $\delta_{3:1}$ , is given by

$$\delta_{3:1} = \frac{\varepsilon \sigma}{8}. \quad (41)$$

If initial conditions for  $v_1$  are taken into account while solving (39), (41) is correct up to  $\mathcal{O}(\varepsilon)$ . Moreover, the expression in (41) indicates that the undesirable third-order harmonic is directly proportional to  $\varepsilon$ . This aspect will also be leveraged in the design of the oscillator capacitance  $C$  in Section III-C.

### III. DESIGN SPECIFICATIONS AND PARAMETER SELECTION FOR VO-CONTROLLED INVERTERS

In this section, we outline a procedure to determine the Van der Pol oscillator parameters such that the VO-controlled inverter satisfies a set of ac performance specifications. The virtual-oscillator parameters to be determined are summarized in Table I below. We divide the parameters into i) *scaling factors*  $\kappa_v$  and  $\kappa_i$  (addressed in Section III-A), ii) *voltage-regulation parameters*  $\sigma$  and  $\alpha$  (addressed in Section III-B), and iii) *harmonic-oscillator parameters*  $L$  and  $C$  (addressed in Section III-C).

<sup>1</sup>Functions  $\tau \sin(\tau + \rho_0)$  and  $\tau \cos(\tau + \rho_0)$  grow without bound, and their existence would suggest that  $v$  is unbounded [see (27)]. However, this contradicts the fact that the unforced Van der Pol oscillator has a stable limit cycle with finite radius.

TABLE I  
VOC PARAMETERS

| Symbol     | Description                         | Value                 | Units            |
|------------|-------------------------------------|-----------------------|------------------|
| $\kappa_v$ | Voltage-scaling factor              | 126                   | V/V              |
| $\kappa_i$ | Current-scaling factor              | 0.15                  | A/A              |
| $\sigma$   | Conductance                         | 6.09                  | $\Omega^{-1}$    |
| $\alpha$   | Coefficient of cubic current source | 4.06                  | A/V <sup>3</sup> |
| $C$        | Harmonic-oscillator capacitance     | 0.18                  | F                |
| $L$        | Harmonic-oscillator inductance      | $3.99 \times 10^{-5}$ | H                |

The performance specifications which the parameters are designed to satisfy include the open-circuit voltage  $\bar{V}_{oc}$ ; rated real-power output and corresponding voltage  $\bar{P}_{rated}$  and  $\bar{V}_{min}$ , respectively; rated reactive-power output  $|\bar{Q}_{rated}|$ ; maximum-permissible frequency deviation, rise time, and ratio of the amplitude of the third harmonic to the fundamental  $|\Delta\omega|_{max}$ ,  $t_{rise}^{max}$ , and  $\delta_{3:1}^{max}$ , respectively.

*Candidate design [specifications]:* Accompanying the design strategy to pick system parameters, we present a running example corresponding to the set of performance specifications in Table II. The specifications result in voltage regulation of  $\pm 5\%$  around a nominal voltage of 120 V, and frequency-regulation of  $\pm 0.5$  Hz around a nominal frequency of 60 Hz. The design is subsequently implemented in the hardware prototype discussed in Section IV.  $\square$

#### A. Design of Scaling Factors $\kappa_v$ and $\kappa_i$

Notice from Fig. 2 that the parameters  $\kappa_v$  and  $\kappa_i$ , respectively, determine the voltage and current scaling between the physical-inverter terminal voltage and output current, and those of the virtual-oscillator circuit. To standardize design, we choose  $\kappa_v$  such that when the VO capacitor voltage is 1 V RMS, the inverter-terminal voltage is equal to the open-circuit voltage  $\bar{V}_{oc}$ . Furthermore, we pick  $\kappa_i$  such that when the VO output current is 1 A, the inverter is loaded to full rated capacity  $\bar{P}_{rated}$ . The values of  $\kappa_v$  and  $\kappa_i$  that ensure this are

$$\kappa_v := \bar{V}_{oc}, \quad \kappa_i := \frac{\bar{V}_{min}}{\bar{P}_{rated}}. \quad (42)$$

A system of inverters with different power ratings connected in parallel share the load power in proportion to their ratings if the current gains are chosen as suggested by (42) [4], [5]. This directly follows as a consequence of (19) since  $\kappa_i \bar{P}_{eq}$  is constant in the parallel configuration, and therefore,  $\bar{P}_{eq}/\bar{P}_{rated}$  is the same for each inverter with identical voltage drops across each output impedance.

*Candidate design [scaling factors]:* The specifications call for an open-circuit voltage  $\bar{V}_{oc} = 126$  V. This translates to a voltage-scaling factor  $\kappa_v = 126$  V/V. From the rated power and corresponding voltage  $\bar{P}_{rated} = 750$  W and  $\bar{V}_{min} = 114$  V, we get the current-scaling factor  $\kappa_i = 114/750 = 0.152$  A/A.  $\square$

#### B. Design of Voltage-Regulation Parameters $\sigma$ and $\alpha$

Here, we use the closed-form expression for the voltage-regulation characteristic in (19) to design the VO conductance

TABLE II  
AC PERFORMANCE SPECIFICATIONS

| Symbol                 | Description                           | Value      | Units   |
|------------------------|---------------------------------------|------------|---------|
| $\bar{V}_{oc}$         | Open-circuit voltage                  | 126        | V (RMS) |
| $\bar{P}_{rated}$      | Rated real power                      | 750        | W       |
| $\bar{V}_{min}$        | Voltage at rated power                | 114        | V (RMS) |
| $ \bar{Q}_{rated} $    | Rated reactive power                  | 750        | VARs    |
| $\omega^*$             | Nominal system frequency              | $2\pi 60$  | rad/s   |
| $ \Delta\omega _{max}$ | Maximum frequency offset              | $2\pi 0.5$ | rad/s   |
| $t_{rise}^{max}$       | Rise time (25)                        | 0.2        | s       |
| $\delta_{3:1}^{max}$   | Ratio of third-to-first harmonic (41) | 2          | %       |

$\sigma$  and the cubic coefficient of the nonlinear voltage-dependent current source  $\alpha$ . Effectively, the design strategy suggested below ensures that the equilibrium RMS terminal voltage of the inverter  $\bar{V}_{eq}$  is bounded between the limits:  $\bar{V}_{oc} \geq \bar{V}_{eq} \geq \bar{V}_{min}$ , as the average real-power output  $\bar{P}_{eq}$  is varied between the limits:  $0 \leq \bar{P}_{eq} \leq \bar{P}_{rated}$ .

First, notice from (22) that the choice of  $\kappa_v$  in (42) implies that  $\alpha$  is related to  $\sigma$  through

$$\alpha = \frac{2\sigma}{3}. \quad (43)$$

Next, substituting  $\bar{P}_{eq} = \bar{P}_{rated}$  and  $\bar{V}_{eq} = \bar{V}_{min}$  into the high-voltage solution of (19), we have

$$\bar{V}_{min} = \kappa_v \left( \frac{\sigma + \sqrt{\sigma^2 - 6\alpha(\kappa_i/\kappa_v)\bar{P}_{rated}}}{3\alpha} \right)^{\frac{1}{2}}. \quad (44)$$

Substituting for  $\kappa_v$  and  $\kappa_i$  from (42) and for  $\alpha$  from (43)

$$\bar{V}_{min} = \bar{V}_{oc} \left( \frac{\sigma + \sqrt{\sigma^2 - 4\sigma(\bar{V}_{min}/\bar{V}_{oc})}}{2\sigma} \right)^{\frac{1}{2}}. \quad (45)$$

Solving for  $\sigma$  above, we get

$$\sigma = \frac{\bar{V}_{oc}}{\bar{V}_{min}} \frac{\bar{V}_{oc}^2}{\bar{V}_{oc}^2 - \bar{V}_{min}^2}. \quad (46)$$

The choice of  $\alpha$  and  $\sigma$  in (43) and (46), respectively, inherently establish the critical power value  $\bar{P}_{cr}$  in (20). The design has to be iterated if the margin of difference between the rated and critical power values is insufficient.

*Candidate design [voltage-regulation parameters]:* From the RMS open-circuit and rated-voltage values  $\bar{V}_{oc} = 126$  V and  $\bar{V}_{min} = 114$  V, applying (46) we get  $\sigma = 6.09 \Omega^{-1}$ , and from (43), we have  $\alpha = 4.06$  A/V<sup>3</sup>. The resulting voltage-regulation curve for these design specifications is illustrated in Fig. 4. The inverter is designed to operate in the voltage regime,  $\bar{V}_{oc} \geq \bar{V}_{eq} \geq \bar{V}_{min}$ ; in Appendix B, we show that equilibria corresponding to  $\bar{V}_{eq} > \bar{V}_{cr}$  are locally exponentially stable.  $\square$

#### C. Design of Harmonic-oscillator Parameters $C$ and $L$

Here, we leverage expressions for i) the frequency-regulation characteristic (23), ii) the rise time (25), and iii) the ratio of amplitudes of the third harmonic to the fundamental (41) to

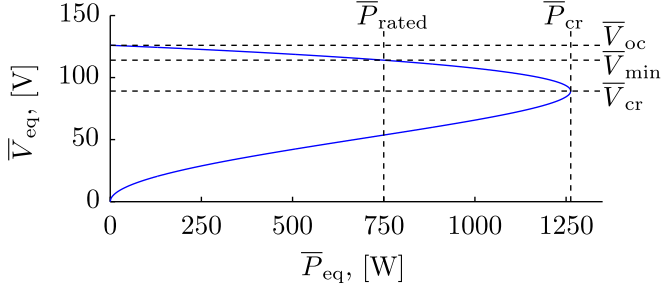


Fig. 4. Equilibrium terminal voltage  $\bar{V}_{eq}$  as a function of the real-power output  $\bar{P}_{eq}$  for the oscillator parameters listed in Table I.

obtain a set of design constraints for the harmonic-oscillator parameters, i.e., the capacitance  $C$  and inductance  $L$ .

Begin with the equilibrium frequency analysis in Section II-B and the frequency-regulation characteristic in (23). The maximum permissible frequency deviation, denoted by  $|\Delta\omega|_{\max}$ , is a design input. Substituting for  $\kappa_v$  and  $\kappa_i$  from (42) into (23), and considering the worst-case operating condition for the terminal voltage,<sup>2</sup> we get the following lower bound on the capacitance  $C$ :

$$C \geq \frac{1}{2|\Delta\omega|_{\max}} \frac{\bar{V}_{oc}}{\bar{V}_{\min}} \frac{|\bar{Q}_{\text{rated}}|}{\bar{P}_{\text{rated}}} =: C_{|\Delta\omega|_{\max}}^{\min} \quad (47)$$

where  $\bar{Q}_{\text{rated}}$  is the maximum average reactive power that can be sourced or consumed by the VO-controlled inverter.

Next, consider the analysis of the (open-circuit) voltage amplitude dynamics in Section II-C, and the expression for the rise time in (25). With the maximum-permissible rise time  $t_{\text{rise}}^{\max}$ , serving as a design input, from (25) and (46), we get the following upper bound for the capacitance  $C$ :

$$C \leq \frac{t_{\text{rise}}^{\max}}{6} \frac{\bar{V}_{oc}}{\bar{V}_{\min}} \frac{\bar{V}_{oc}^2}{\bar{V}_{oc}^2 - \bar{V}_{\min}^2} =: C_{t_{\text{rise}}^{\max}}^{\max}. \quad (48)$$

Finally, consider the harmonics analysis in Section II-D, and the expression for the ratio of the amplitudes of the third harmonic to the fundamental in (41). With the maximum-permissible ratio  $\delta_{3:1}^{\max}$ , serving as a design input, from (41) and (46), we get an additional lower bound on the capacitance  $C$

$$C \geq \left( \frac{1}{8\omega^* \delta_{3:1}^{\max}} \right) \frac{\bar{V}_{oc}}{\bar{V}_{\min}} \frac{\bar{V}_{oc}^2}{\bar{V}_{oc}^2 - \bar{V}_{\min}^2} =: C_{\delta_{3:1}^{\max}}^{\min}. \quad (49)$$

Once a value of capacitance satisfying (47)–(49) is selected, the inductance  $L$  follows from rearranging terms in (10)

$$L = \frac{1}{C(\omega^*)^2}. \quad (50)$$

Combining (47)–(49), we get the following range in which  $C$  must be selected to meet the performance specifications of frequency regulation, rise time, and harmonics

$$\max \left\{ C_{|\Delta\omega|_{\max}}^{\min}, C_{\delta_{3:1}^{\max}}^{\min} \right\} \leq C \leq C_{t_{\text{rise}}^{\max}}^{\max}. \quad (51)$$

<sup>2</sup>This corresponds to consuming or sourcing the maximum reactive power at the minimum permissible terminal voltage,  $\bar{V}_{\min}$ , which is defined in (45).

If  $C_{t_{\text{rise}}^{\max}}^{\max} < \max \{ C_{|\Delta\omega|_{\max}}^{\min}, C_{\delta_{3:1}^{\max}}^{\min} \}$ , then it is not possible to simultaneously meet the specifications of frequency regulation, rise time, and harmonics. Therefore, (51) reveals a fundamental tradeoff in specifying performance requirements and designing VO-controlled inverters. In particular, a VO-controlled inverter that offers a short rise time will necessarily have a larger frequency offset and harmonic distortion, while a tightly regulated VO-controlled inverter (smaller frequency offset and harmonic distortion) will necessarily have a longer rise time.

*Candidate design [harmonic-oscillator parameters]:* For our example VO-controlled inverter, we have selected the ac performance specifications  $|\Delta\omega|_{\max} = 2\pi 0.5 \text{ rad/s}$ ,  $t_{\text{rise}}^{\max} = 0.2 \text{ s}$ , and  $\delta_{3:1}^{\max} = 2\%$  (see Table II). Substituting these into (47)–(49), we find that  $C_{|\Delta\omega|_{\max}}^{\min} = 0.1759 \text{ F}$ ,  $C_{t_{\text{rise}}^{\max}}^{\max} = 0.2031 \text{ F}$ , and  $C_{\delta_{3:1}^{\max}}^{\min} = 0.1010 \text{ F}$ . Therefore, to meet the performance specifications, we must select the harmonic-oscillator capacitance  $C$  in the range  $0.1759 \text{ F} \leq C \leq 0.2031 \text{ F}$ . Without loss of generality, prioritizing the rise-time specification, we will select  $C$  at the lower bound of the specified range, i.e.,  $C = 0.1759 \text{ F}$ . Since  $\omega^* = 2\pi 60 \text{ rad/s}$ , it then follows from (50) that  $L = 39.99 \mu\text{H}$ .

In closing, we remark that the voltage- and frequency-regulation specifications for the inverter are given here in terms of worst-case limits. Given the ubiquity of droop control in this domain, they could be specified in terms of the active- and reactive-power droop coefficients  $m_P$  and  $m_Q$  respectively. Leveraging the correspondences in (54) and (55), we comment next on how the design procedure above (for the scaling, voltage regulation, and harmonic-oscillator parameters) can be modified to ensure that the VO-controlled inverter mimics a droop-controlled inverter with the specified  $m_P$  and  $m_Q$ .

#### D. Comparison With Droop Control

For resistive distribution lines, droop control linearly trades off the inverter terminal-voltage amplitude versus active power and inverter frequency versus reactive power. In the context of the notation established above, these linear laws can be expressed as

$$\bar{V}_{eq} = \bar{V}_{oc} + m_P \bar{P}_{eq}, \quad (52)$$

$$\omega_{eq} = \omega^* + m_Q \bar{Q}_{eq}, \quad (53)$$

where  $m_P < 0$  is the active-power droop coefficient and  $m_Q > 0$  is the reactive-power droop coefficient [26]. In fact, it is shown in [27] that the relations in (52) and (53) provide robust performance for various types of line impedances and are, thus, referred to as *universal droop* laws. In our previous work [5], we observed that the equilibria of the averaged VOC dynamics in (15) and (16) can be engineered to be in close correspondence with the droop laws in (52) and (53). For instance, a first-order expansion of  $\bar{V}_{eq}$  (as a function of  $\bar{P}_{eq}$ ) around the open-circuit voltage  $\bar{V}_{oc}$  is of the form (52) with the following choice of  $m_P$ :

$$m_P = \frac{\kappa_v \kappa_i}{2\sigma} \left( \bar{V}_{oc} - \beta \bar{V}_{oc}^3 \right)^{-1}. \quad (54)$$

This expression can be derived by evaluating  $d\bar{V}_{eq}/d\bar{P}_{eq}$  from (18) at the open-circuit voltage  $\bar{V}_{oc}$ . Similarly, by



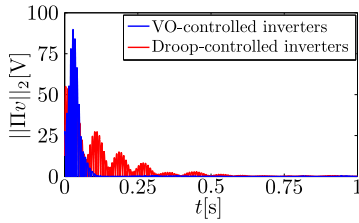


Fig. 5. Synchronization error, captured from the deviation of the inverter terminal voltages from the average, as a function of time for VOC and droop control. The waveforms are obtained from switching-level simulations.

inspecting (23), we see that  $\omega_{eq}$  as a function of  $\bar{Q}_{eq}$  around the open-circuit voltage,  $\bar{V}_{oc}$ , is of the form (53) with the following choice of  $m_Q$ :

$$m_Q = \frac{\kappa_v \kappa_i}{2C\bar{V}_{oc}^2}. \quad (55)$$

With the design strategy proposed in Section III for the parameters  $C$ ,  $\kappa_v$ ,  $\kappa_i$ ,  $\alpha$ , and  $\sigma$ , it emerges that the voltage-regulation characteristic in (19) and the frequency-regulation characteristic in (23) are close to linear over a wide load range. The experimental results in Section IV (see Figs. 8 and 9) validate this claim; conclusively demonstrating that droop laws are embedded within the equilibria of the nonlinear VOC dynamics. This establishes the backward compatibility of VOC, in that it subsumes droop control in sinusoidal steady state.<sup>3</sup>

We also consider the converse scenario where droop coefficients  $m_P$  and  $m_Q$  are translated into VOC parameters. The choice of  $\kappa_v$ ,  $\kappa_i$  [as given by (42)], and  $\alpha$  [as given by (43)] would remain unchanged. With regard to  $\sigma$ , from (54) and with  $\beta$  given in (5), we get

$$\sigma = -m_P^{-1} \frac{\kappa_i}{2}. \quad (56)$$

Furthermore, from (55), we see that the choice of capacitance  $C$  would be given by

$$C = m_Q^{-1} \frac{\kappa_i}{2\bar{V}_{oc}}, \quad (57)$$

while the inductance  $L$  would still be specified by (50). Limits on  $C$  can be considered in a similar fashion as before, if the specification on  $m_Q$  is in terms of an upper bound.

Although correspondences between the quasi-steady-state behavior of VOC and droop control exist as outlined above, their time-domain performance is markedly different. The main advantage of VOC is that it is a time-domain controller which acts directly on unprocessed ac measurements when controlling the inverter terminal voltage, as evident in (3). This is unlike droop control which processes ac measurements to compute phasor-based quantities, namely real and reactive power, which are then used to update the inverter voltage amplitude and frequency set

<sup>3</sup>In addition to the droop laws highlighted in (52) and (53), there are other droop laws for different network types. VOC can accommodate arbitrary network impedances by expressing the inverter terminal voltage as  $v = x \sin \varphi + y \cos \varphi$ , where  $x = \kappa_v \varepsilon i_L$ ,  $y = \kappa_v v_C$ , and  $\varphi$  can be interpreted as an angular rotation in the polar plane [28]. With this setting, it can be shown that  $\varphi = \pi/2$  yields the droop laws for inductive networks. For the remainder of this paper, we focus on the case where  $\varphi = 0$ .

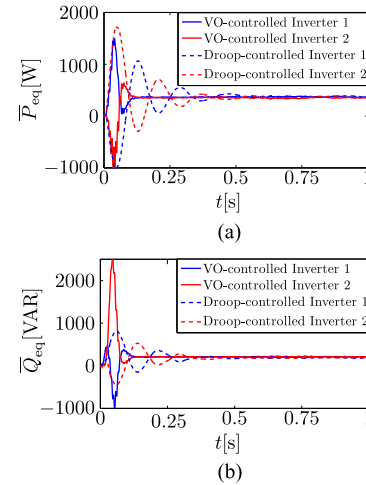


Fig. 6. Active- and reactive-power sharing for the two-inverter case for VOC and droop control.

points. Since phasor quantities are not well defined in real time, droop controllers must necessarily employ a combination of low-pass filters, cycle averaging, coordinate transformations, or  $\pi/2$  delays to compute  $\bar{P}_{eq}$  and  $\bar{Q}_{eq}$  in (52) and (53) (see [17], [29]–[31]). These filters, which typically have a cutoff frequency in the range of 1 to 15 Hz [17], [29], [31], act as a bottleneck to control responsiveness, which in turn cause a sluggish response. In contrast, VO-controlled inverters operate on real-time measurements and respond to disturbances as they occur. To illustrate these concepts, we present a simple case study that demonstrates the time-domain performance of VOC and its power-sharing capabilities.

*Simulation Case Study:* We consider two identical single-phase inverters connected in parallel through resistors to a parallel  $RL$  load and simulate the time-domain behavior of VOC. For comparison, we also illustrate the performance of droop control. For the droop controller implementation, we leverage the droop laws in resistive networks (52), (53) and the control architecture is adopted from [30]. The virtual oscillator that emulates the regulation characteristics is then derived by using the aforementioned analysis [see (56) and (57)].

Fig. 5 depicts the time it takes for two inverters to synchronize starting from arbitrary initial conditions. We make use of a metric  $\|\Pi v\|_2$ , where  $v = [v_1, v_2]^T$  collects terminal voltages at the inverter. The matrix  $\Pi := I_2 - \frac{1}{2} \mathbf{1}_2 \mathbf{1}_2^T$  ( $I_{2 \times 2}$  is the  $2 \times 2$  identity, and  $\mathbf{1}_{2 \times 1}$  is the  $2 \times 1$  vector with all entries equal to one) is the so-called projector matrix, and by construction, we see that  $\Pi v$  returns a vector where the entries capture deviations from the average of the vector  $v$ . From the figure, we see that with VOC, the inverters synchronize by around  $t = 0.1$  s, while with droop control, the inverters synchronize by  $t = 0.6$  s. Furthermore, Fig. 6(a) and (b) shows that identical active- and reactive-power sharing is achieved with both control strategies; it is worth noting, however, that VOC reaches steady state faster than droop. The  $RL$  load considered in this particular setup has values of  $R_{load} = 20 \Omega$  and  $L_{load} = 0.1$  H with interconnecting conductances  $g_{1,line} = 5 \Omega^{-1}$  and  $g_{2,line} = 4 \Omega^{-1}$ , respectively, for inverters 1 and 2. Readers are referred to [28] for other simulation parameters.

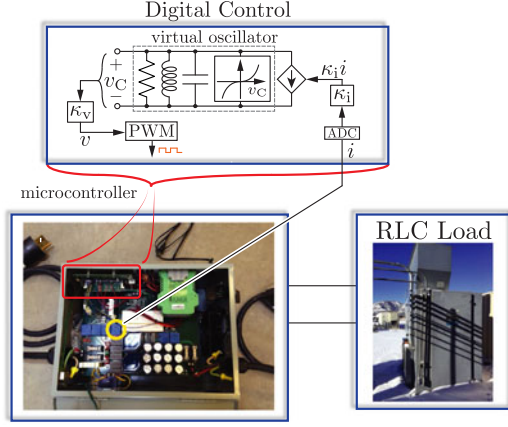


Fig. 7. Picture of laboratory prototype of VO-controlled inverter and load.

#### IV. EXPERIMENTAL VALIDATION

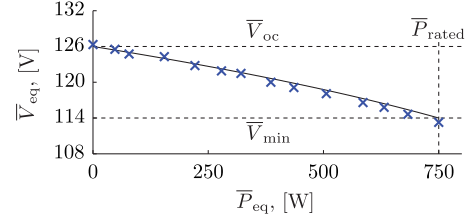
We built a laboratory-scale hardware prototype of a VO-controlled inverter with design specifications in Table II. A picture of the experimental setup is shown in Fig. 7. The scaling, voltage regulation, and harmonic-oscillator parameters—that completely characterize the virtual oscillator and ensure the VO-controlled inverter satisfies the design specifications—were computed in the running example in Section III, and they are listed in Table I. The inverter  $LCL$  filter components have values  $L_f = 600 \mu\text{H}$ ,  $C_f = 24 \mu\text{F}$ , and  $L_g = 44 \mu\text{H}$ , where  $L_f$ ,  $C_f$ , and  $L_g$  are the inverter-side inductor, ac-filter capacitor, and grid-side inductor, respectively (see Fig. 2). The switching frequency of the inverter is  $T_{sw}^{-1} = 15 \text{ kHz}$ , the dead time is  $200 \text{ ns}$ , and a three-level unipolar sine-triangle PWM is utilized. The nonlinear dynamics of the virtual-oscillator circuit are programmed on a Texas Instruments TMS320F28335 microcontroller. A short note on the discretization is provided next.

##### A. Digital Controller Implementation

Denote the sampling time utilized in the numerical integration by  $T_s$ . In this particular implementation, we pick  $T_s^{-1} = 15 \text{ kHz}$ . To discretize the virtual-oscillator dynamics (3), we adopt the trapezoidal rule of integration and recover the following difference equations:

$$\begin{aligned} v[k] &= \left(1 - \frac{T_s \sigma}{2C} + \frac{T_s^2}{4LC}\right)^{-1} \left[ \left(1 + \frac{T_s \sigma}{2C} - \frac{T_s^2}{4LC}\right) v[k-1] \right. \\ &\quad - \frac{T_s}{C} \kappa_v i_L[k-1] - \frac{T_s}{2C} \kappa_v \kappa_i (i[k] + i[k-1]) \\ &\quad \left. - \frac{\alpha T_s}{2C \kappa_v^2} (v^3[k] + v^3[k-1]) \right] \\ i_L[k] &= i_L[k-1] + \frac{T_s}{2L \kappa_v} (v[k] + v[k-1]) \end{aligned} \quad (58)$$

where  $k \in \mathbb{Z}_{\geq 0}$  denotes the  $k$ th sampling instance,  $i[k]$  is the sampled inverter-output current,  $i_L[k]$  is the sampled Van der Pol oscillator inductor current, and  $v[k]$  is the sampled inverter-terminal voltage. The difference equations (58) cannot be directly implemented on a digital controller, since they con-

Fig. 8. Measured versus analytically computed values for steady-state RMS voltage  $\bar{V}_{eq}$  versus output real power  $\bar{P}_{eq}$ .

tain an algebraic loop through the cubic term  $v^3[k]$ . Therefore, it is necessary to make a simplifying assumption to eliminate the algebraic loop. While there are many approaches to accomplish this, one option is to simply make the assumption  $v^3[k] \approx v^3[k-1]$ , allowing (58) to be approximated as

$$\begin{aligned} v[k] &= \left(1 - \frac{T_s \sigma}{2C} + \frac{T_s^2}{4LC}\right)^{-1} \left[ \left(1 + \frac{T_s \sigma}{2C} - \frac{T_s^2}{4LC}\right) v[k-1] \right. \\ &\quad - \frac{T_s}{C} \kappa_v i_L[k-1] - \frac{T_s}{2C} \kappa_v \kappa_i (i[k] + i[k-1]) \\ &\quad \left. - \frac{\alpha T_s}{C \kappa_v^2} v^3[k-1] \right] \\ i_L[k] &= i_L[k-1] + \frac{T_s}{2L \kappa_v} (v[k] + v[k-1]). \end{aligned} \quad (59)$$

The difference equations (59) yield realizable—albeit approximate—dynamics of the virtual oscillator circuit in Fig. 2, and they can be implemented directly on the digital controller. The inverter PWM modulation signal  $m$  can then be constructed as

$$m[k] := \frac{v[k]}{v_{dc}[k]}, \quad (60)$$

where  $v_{dc}[k]$  is the measured value of the inverter dc bus voltage at the  $k$ th sampling instance.

The experimental results that are outlined next focus on validating i) the steady-state voltage-regulation characteristic in (19), ii) the steady-state frequency-regulation characteristic in (23), iii) the expression for the rise time in (25), and iv) the expression for the ratio of the amplitudes of the third and first harmonics in (41). Results are summarized in Figs. 8–11; in each case, the analytical results are plotted as solid lines, while results from experimental studies are plotted as  $\times$ 's.

##### B. Steady-state Voltage Regulation

This experiment is performed with the VO-controlled inverter connected to a variable resistive load at the output terminals. The experimental results reported in Fig. 8 are obtained by varying the load resistance in discrete steps between open circuit and  $16.7 \Omega$ , and in each case, recording the steady-state RMS terminal voltage. The measured data (plotted as  $\times$ 's) match the analytical voltage-regulation characteristic (19) (plotted as a solid line). Note that the inverter RMS voltage stays within the prescribed upper and lower bounds  $\bar{V}_{oc}$  and  $\bar{V}_{min}$ , respectively, across the entire rated load-power range.

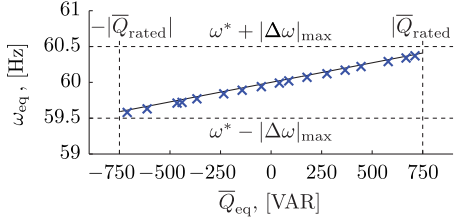


Fig. 9. Measured versus analytically computed values for steady-state frequency  $\omega_{eq}$  versus output reactive power  $\bar{Q}_{eq}$ .

1) *Comparison With Voltage-amplitude Droop Control:* The best-fit linear model (in a least-squares sense) to the experimentally collected values  $\{\bar{V}_{eq}, \bar{P}_{eq}\}$  plotted in Fig. 8 is given by

$$\bar{V}_{eq} = 126.5449 - 0.0171 \bar{P}_{eq}. \quad (61)$$

The coefficient of determination—a metric that reveals the quality of a statistical model [32]—for this linear model is 99.59%. These findings conclusively demonstrate that the voltage-amplitude real-power droop law is embedded within the sinusoidal steady state of VO-controlled inverters, validating our theoretical analysis in [5].

### C. Steady-state Frequency Regulation

The frequency-regulation characteristic in (23) is validated by connecting a variable reactive load to the inverter-output terminals and adjusting it in incremental steps such that the inverter is delivering purely reactive power into either a capacitive or inductive load. The load was varied such that the total reactive power delivered into the *LCL* filter and external load was between  $\pm \bar{Q}_{rated}$  where  $|\bar{Q}_{rated}| = 750$  VAR. In particular, purely inductive loads were varied discretely between 46.9 and 442 mH and capacitive loads were adjusted between 14.9 and 92.7  $\mu$ F. In Fig. 9, we plot the measured steady-state reactive power delivered into the filter and load  $\bar{Q}_{eq}$  and the frequency at the inverter terminals. The solid curve corresponds to the analytically derived expression in (23) when evaluated at  $\bar{V}_{eq} = \bar{V}_{oc}$  (since  $\bar{P}_{eq} \approx 0$  for this particular experiment).

1) *Comparison With Frequency Droop Control:* The best-fit linear model to the experimentally collected values  $\{\omega_{eq}, \bar{Q}_{eq}\}$  plotted in Fig. 9 is given by

$$\omega_{eq} = 376.8013 + 0.0035 \bar{Q}_{eq}. \quad (62)$$

The coefficient of determination for this linear model is 99.98%. Again, these observations demonstrate that the frequency-reactive power droop law is intrinsically embedded in the sinusoidal steady-state behavior of VO-controlled inverters, further validating our theoretical analysis in [5].

### D. Harmonics

We now validate the expression for the ratio of the amplitude of the third harmonic to the fundamental  $\delta_{3:1}$  in (41). In this experiment, the parameters *L* and *C* of the inverter VOC controller were adjusted so that  $\varepsilon = \sqrt{L/C}$  varies, while  $\omega^* = 1/\sqrt{LC}$  remains constant at  $2\pi 60$  rad/s. All other parameters are held fixed to the nominal values in Table I. The 'x's' in Fig. 10 represent experimentally collected values of  $\delta_{3:1}$  as a function of  $\varepsilon$ ,

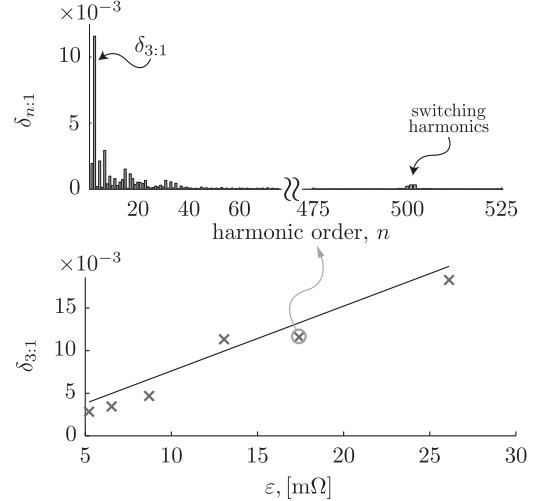


Fig. 10. Measured versus analytically computed values of the ratio of the third harmonic amplitude and the fundamental amplitude  $\delta_{3:1}$  as a function of  $\varepsilon$ . Inset depicts higher order harmonics for a particular value of  $\varepsilon$ .

while the solid line follows from the expression in (41). The inset for a particular measurement confirms that the third harmonic is dominant over all others.

### E. Rise Time

Finally, we validate the expression for the rise time  $t_{rise}$  in (25) (recall this is the time for the open-circuit inverter terminal-voltage magnitude to rise from 10% to 90% of its steady-state value  $\bar{V}_{eq} = \bar{V}_{oc}$ ). The same sweep of the VOC parameters *L* and *C* as in Section IV-D is used here, with all other parameters fixed to the nominal values in Table I. The 'x's' in Fig. 11 represent measured values of the rise time for each value of  $\varepsilon$ , while the solid line follows from the analytic expression (25).

*Remark:* The harmonics and rise-time experiments in Sections IV-D and IV-E report voltage measurements collected at the filter capacitor *C<sub>f</sub>*, i.e., the voltage *v<sub>f</sub>* in Fig. 2. Since the *L<sub>f</sub>C<sub>f</sub>* filter is solely designed to attenuate switching harmonics, in effect, the low-frequency and slow-time-scale behavior of the voltage *v<sub>f</sub>* matches that of the inverter terminal voltage *v*, for which the harmonics and rise-time analysis is performed in Sections II-D and II-C. In particular, since the corner frequency of the *L<sub>f</sub>C<sub>f</sub>* low-pass filter  $1/\sqrt{L_f C_f} = 8.33 \times 10^3$  rad/s  $\gg \omega^* = 377$  rad/s, and the open-circuit voltage builds up over multiple ac cycles, the rise time of *v<sub>f</sub>* closely mirrors that of the inverter terminal voltage *v*. Furthermore, since  $|v_f(j\omega)|/|\tilde{v}(j\omega)| = \|(j\omega C_f)^{-1}/((j\omega C_f)^{-1} + j\omega L_f)\|_2$  evaluated at  $\omega^*$  and  $3\omega^*$  is approximately equal to 1.0021 and 1.0018,  $\delta_{3:1}$  can be computed from measurements of *v<sub>f</sub>* without compromising accuracy.

## V. CONCLUDING REMARKS AND DIRECTIONS FOR FUTURE WORK

In this paper, we considered the performance and design of VO-controlled inverters. Leveraging notions from periodic averaging of weakly nonlinear systems, we derived the phasor-domain amplitude and phase dynamics of VO-controlled

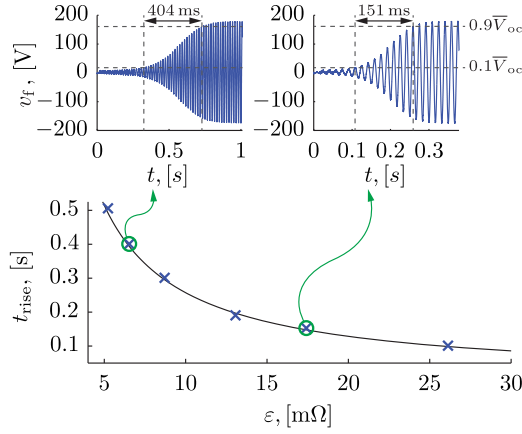


Fig. 11. Measured versus analytically computed values of rise time  $t_{\text{rise}}$  as a function of  $\varepsilon$ . Insets depict time-domain waveforms of the inverter terminal voltage for two different values of  $\varepsilon$ .

inverters. These were used to obtain the steady-state voltage- and frequency-regulation characteristics. Furthermore, we also quantified the dynamic response and harmonics in VO-controlled inverters. The analytical approach was leveraged to develop a design procedure through which a VO-controlled inverter can be guaranteed to meet a specified set of ac performance specifications. The analytical expressions were validated by experiments. As a part of future work, we plan to further explore correspondences with droop control laws and expand on the set of performance specifications that VO-controlled inverters can be designed for. We also plan to analyze the interoperability of a heterogeneous collection of droop- and VO-controlled inverters connected in a microgrid network from dynamic and steady-state standpoints. The analytical approach to compute the rise time and harmonic content is performed with an unloaded inverter. Including detailed load dynamics in these analyses is also a key direction for future work. Finally, while our experimental results and analyses demonstrate that the steady-state behavior of VOC can be engineered to be in close concert with droop control, similar comparative studies from the perspective of transient behaviors are a part of ongoing investigations.

## APPENDIX

### A. Derivation of Averaged Model in (15) and (16)

In the forthcoming analysis, we will find the following definition of the angular dynamics of the inverter terminal voltage useful

$$\frac{d}{dt}\phi = \omega^* + \frac{d}{dt}\theta^* = \omega + \frac{d}{dt}\theta, \quad (63)$$

where  $\phi$  is the instantaneous phase angle corresponding to the inverter sinusoidal output,  $\omega^*$  is the nominal (open-circuit) frequency of the inverter ac output, and  $\omega$  represents the (load-dependent) system frequency in quasi-stationary sinusoidal steady state. The angles  $\theta^*$  and  $\theta$  represent phase offsets with respect to the rotating reference frames established by  $\omega^*$  and  $\omega$ , respectively. With the definition established in (63), the inverter

terminal voltage in (4) can be equivalently written as

$$v(t) = \sqrt{2}V(t) \cos(\omega^*t + \theta^*(t)). \quad (64)$$

Recalling that the inverter output current is denoted by  $i(t)$ , we define the instantaneous real- and reactive-power injections [33], [34] as

$$P(t) = v(t)i(t), \quad Q(t) = v\left(t - \frac{\pi}{2}\right)i(t). \quad (65)$$

The average real and reactive power over an ac cycle of period  $2\pi/\omega^*$  are then given by

$$\bar{P} = \frac{\omega^*}{2\pi} \int_{s=0}^{2\pi/\omega^*} P(s)ds, \quad \bar{Q} = \frac{\omega^*}{2\pi} \int_{s=0}^{2\pi/\omega^*} Q(s)ds. \quad (66)$$

To obtain (15) and (16) from (9), begin by expressing (9) with respect to  $\theta^*$

$$\begin{aligned} \dot{V} &= \frac{\varepsilon}{\sqrt{2}} \left( \sigma g(\sqrt{2}V \cos(\tau + \theta^*)) - \kappa_v \kappa_i i \right) \cos(\tau + \theta^*), \\ \dot{\theta}^* &= -\frac{\varepsilon}{\sqrt{2}V} \left( \sigma g(\sqrt{2}V \cos(\tau + \theta^*)) - \kappa_v \kappa_i i \right) \sin(\tau + \theta^*). \end{aligned} \quad (67)$$

The dynamical systems above are  $2\pi$ -periodic functions in  $\tau$ . In the quasi-harmonic limit  $\varepsilon \searrow 0$ , following (12), we obtain the averaged dynamics:

$$\begin{aligned} \begin{bmatrix} \dot{\bar{V}} \\ \dot{\bar{\theta}}^* \end{bmatrix} &= \frac{\varepsilon\sigma}{2\pi\sqrt{2}} \int_0^{2\pi} g(\sqrt{2}\bar{V} \cos(\tau + \bar{\theta}^*)) \begin{bmatrix} \cos(\tau + \bar{\theta}^*) \\ -\frac{1}{\bar{V}} \sin(\tau + \bar{\theta}^*) \end{bmatrix} d\tau, \\ &\quad - \frac{\varepsilon\kappa_v \kappa_i}{2\pi\sqrt{2}} \int_0^{2\pi} i \begin{bmatrix} \cos(\tau + \bar{\theta}^*) \\ -\frac{1}{\bar{V}} \sin(\tau + \bar{\theta}^*) \end{bmatrix} d\tau \\ &= \frac{\varepsilon\sigma}{2} \begin{bmatrix} \bar{V} - \frac{\beta}{2}\bar{V}^3 \\ 0 \end{bmatrix} - \frac{\varepsilon\kappa_v \kappa_i}{2\pi\sqrt{2}} \int_0^{2\pi} i \begin{bmatrix} \cos(\tau + \bar{\theta}^*) \\ -\frac{1}{\bar{V}} \sin(\tau + \bar{\theta}^*) \end{bmatrix} d\tau. \end{aligned} \quad (68)$$

Transitioning (68) from  $\tau$  to  $t$  coordinates and retaining only  $\mathcal{O}(\varepsilon)$  terms, we get

$$\begin{aligned} \frac{d}{dt} \begin{bmatrix} \bar{V} \\ \bar{\theta}^* \end{bmatrix} &= \frac{\sigma}{2C} \begin{bmatrix} \bar{V} - \frac{\beta}{2}\bar{V}^3 \\ 0 \end{bmatrix} \\ &\quad - \frac{\kappa_v \kappa_i \omega^*}{2\pi\sqrt{2}C} \int_0^{\frac{2\pi}{\omega^*}} i(t) \begin{bmatrix} \cos(\omega^*t + \bar{\theta}^*) \\ -\frac{1}{\bar{V}} \sin(\omega^*t + \bar{\theta}^*) \end{bmatrix} dt, \\ &= \frac{\sigma}{2C} \begin{bmatrix} \bar{V} - \frac{\beta}{2}\bar{V}^3 \\ 0 \end{bmatrix} \\ &\quad + \frac{\kappa_v \kappa_i \omega^*}{4\pi C} \int_0^{\frac{2\pi}{\omega^*}} \begin{bmatrix} -\frac{1}{\bar{V}} \sqrt{2}V(t)i(t) \cos(\omega^*t + \theta^*) \\ \frac{1}{\bar{V}^2} \sqrt{2}V(t)i(t) \sin(\omega^*t + \theta^*) \end{bmatrix} dt. \end{aligned} \quad (69)$$



Recalling the definitions of the instantaneous real and reactive power in (65), we get

$$\frac{d}{dt} \begin{bmatrix} \bar{V} \\ \bar{\theta}^* \end{bmatrix} = \frac{\sigma}{2C} \begin{bmatrix} \bar{V} - \frac{\beta}{2} \bar{V}^3 \\ 0 \end{bmatrix} + \frac{\kappa_v \kappa_i \omega^*}{4\pi C} \int_0^{\frac{2\pi}{\omega^*}} \begin{bmatrix} -\frac{P(t)}{\bar{V}} \\ \frac{Q(t)}{\bar{V}^2} \end{bmatrix} dt, \quad (70)$$

from which we recover the averaged dynamics in (15) and (16). For further details on the derivation above, see [5].

### B. Stability of High-Voltage Solution to (18)

The voltage- and frequency-regulation characteristics outlined in Section II-B help to quantify the *large-signal* sensitivity of the approach to load variations. From a *small-signal* perspective, we show next that the high-voltage root in (19) is locally asymptotically stable. Consider the averaged amplitude and phase dynamics in (15) and (16). We can capture the voltage-amplitude and phase dependence of the real- and reactive-power output by describing them as  $\bar{P} := p(\bar{V}, \bar{\theta})$  and  $\bar{Q} := q(\bar{V}, \bar{\theta})$ , respectively. Linearizing (15) and (16) around an equilibrium point  $(\bar{V}_{eq}, \bar{\theta}_{eq})$ , we get the following entries for the Jacobian matrix  $J \in \mathbb{R}^{2 \times 2}$  of the linearized system:

$$\begin{aligned} [J]_{1,1} &= \frac{\sigma}{2C} \left( 1 - \frac{3\beta}{2} \bar{V}_{eq}^2 \right) + \frac{\kappa_v \kappa_i}{2C \bar{V}_{eq}^2} p(\bar{V}_{eq}, \bar{\theta}_{eq}) \\ &\quad - \frac{\kappa_v \kappa_i}{2C \bar{V}_{eq}} \frac{\partial p(\bar{V}_{eq}, \bar{\theta}_{eq})}{\partial \bar{V}} \\ [J]_{1,2} &= -\frac{\kappa_v \kappa_i}{2C \bar{V}_{eq}} \frac{\partial p(\bar{V}_{eq}, \bar{\theta}_{eq})}{\partial \bar{\theta}} \\ [J]_{2,1} &= -\frac{\kappa_v \kappa_i}{\bar{V}_{eq}^3} + \frac{\kappa_v \kappa_i}{2C \bar{V}_{eq}^2} \frac{\partial q(\bar{V}_{eq}, \bar{\theta}_{eq})}{\partial \bar{V}} \\ [J]_{2,2} &= \frac{\kappa_v \kappa_i}{2C \bar{V}_{eq}^2} \frac{\partial q(\bar{V}_{eq}, \bar{\theta}_{eq})}{\partial \bar{\theta}}. \end{aligned} \quad (71)$$

To analyze the stability of a nonzero amplitude equilibrium, we assume the following to decouple the linearized amplitude dynamics from the phase dynamics:

$$\frac{\partial p(\bar{V}_{eq}, \bar{\theta}_{eq})}{\partial \bar{\theta}} = 0. \quad (72)$$

Note that this is a standard decoupling power-flow approximation widely used in resistive networks. With the decoupling assumption, the stability of the averaged amplitude dynamics can be guaranteed if we ensure

$$\begin{aligned} [J]_{1,1} &= \frac{\sigma}{2C} \left( 1 - \frac{3\beta}{2} \bar{V}_{eq}^2 \right) + \frac{\kappa_v \kappa_i}{2C \bar{V}_{eq}^2} p(\bar{V}_{eq}, \bar{\theta}_{eq}) \\ &\quad - \frac{\kappa_v \kappa_i}{2C \bar{V}_{eq}} \frac{\partial p(\bar{V}_{eq}, \bar{\theta}_{eq})}{\partial \bar{V}} < 0. \end{aligned} \quad (73)$$

Now, consider a particular load for which the average power over a cycle is constant, i.e.,

$$\bar{P} = p(\bar{V}, \bar{\theta}) = \bar{P}_{eq}. \quad (74)$$

Notice that this load satisfies the decoupling requirement in (72). Recall that we have two possible equilibrium voltage solutions to (18), given by

$$\bar{V}_{eq}^{\text{low}} = \kappa_v \left( \frac{\sigma - \sqrt{\sigma^2 - 6\alpha(\kappa_i/\kappa_v)\bar{P}_{eq}}}{3\alpha} \right)^{\frac{1}{2}}, \quad (75)$$

$$\bar{V}_{eq}^{\text{high}} = \kappa_v \left( \frac{\sigma + \sqrt{\sigma^2 - 6\alpha(\kappa_i/\kappa_v)\bar{P}_{eq}}}{3\alpha} \right)^{\frac{1}{2}}. \quad (76)$$

The stability condition from (73) suggests that the stable equilibrium RMS voltage satisfies

$$\frac{3\sigma\beta}{2} \bar{V}_{eq}^4 - \sigma \bar{V}_{eq}^2 - \kappa_v \kappa_i \bar{P}_{eq} > 0. \quad (77)$$

For  $\bar{P}_{eq} > 0$ , (77) holds for all values of  $\bar{V}_{eq}$  that satisfy

$$\begin{aligned} \bar{V}_{eq} &> \left( \frac{\sigma + \sqrt{\sigma^2 + 6\kappa_v \kappa_i \sigma \beta \bar{P}_{eq}}}{3\sigma\beta} \right)^{\frac{1}{2}} \\ &= \kappa_v \left( \frac{\sigma + \sqrt{\sigma^2 + 18(\kappa_i/\kappa_v)\alpha \bar{P}_{eq}}}{9\alpha} \right)^{\frac{1}{2}} =: \bar{V}_{\text{lim}}, \end{aligned} \quad (78)$$

where in the last line in (78),  $\beta$  is substituted in terms of  $\alpha$  using (5). The stable equilibrium is the one that satisfies (78). Since we assume the existence of solutions *a priori*, this implies that  $\bar{P}_{eq} < \bar{P}_{cr}$ , with  $\bar{P}_{cr}$  specified in (20). Subsequently, we can bound  $\bar{V}_{\text{lim}}$  as follows:

$$\bar{V}_{\text{lim}} < \kappa_v \left( \frac{\sigma + \sqrt{\sigma^2 + 3\sigma^2}}{9\alpha} \right)^{\frac{1}{2}} = \kappa_v \sqrt{\frac{\sigma}{3\alpha}} = \bar{V}_{cr}. \quad (79)$$

Finally, note that among the possible equilibria in (75) and (76),  $\bar{V}_{eq}^{\text{high}} > \bar{V}_{cr}$ ; and from (79), it follows that  $\bar{V}_{eq}^{\text{high}} > \bar{V}_{\text{lim}}$ . Thus, the high-voltage solution is locally asymptotically stable.

### REFERENCES

- [1] M. C. Chandorkar, D. M. Divan, and R. Adapa, "Control of parallel connected inverters in standalone AC supply systems," *IEEE Trans. Ind. Appl.*, vol. 29, no. 1, pp. 136–143, Jan. 1993.
- [2] L. A. B. Tôres, J. P. Hespanha, and J. Moehlis, "Power supplies synchronization without communication," presented at the Power Energy Society General Meeting, San Diego, CA, USA, Jul. 2012.
- [3] L. A. B. Tôres, J. P. Hespanha, and J. Moehlis, "Synchronization of identical oscillators coupled through a symmetric network with dynamics: A constructive approach with applications to parallel operation of inverters," *IEEE Trans. Automat. Control.*, to be published.
- [4] B. B. Johnson, S. V. Dhople, A. O. Hamadeh, and P. T. Krein, "Synchronization of parallel single-phase inverters with virtual oscillator control," *IEEE Trans. Power Electron.*, vol. 29, no. 11, pp. 6124–6138, Nov. 2014.
- [5] M. Sinha, F. Dörfler, B. B. Johnson, and S. V. Dhople, "Uncovering droop control laws embedded within the nonlinear dynamics of Van der Pol oscillators," *IEEE Trans. Control Network Syst.*, 2015, in press.
- [6] S. E. Tuna, "Synchronization analysis of coupled Liénard-type oscillators by averaging," *Automatica*, vol. 48, no. 8, pp. 1885–1891, 2012.
- [7] H. K. Khalil, *Nonlinear Systems*, 3ed. Englewood Cliffs, NJ, USA: Prentice-Hall, 2002.
- [8] A. H. Nayfeh, *Introduction to Perturbation Techniques*. Hoboken, NJ, USA: Wiley, 2011.
- [9] F. Dörfler and F. Bullo, "Synchronization in complex oscillator networks: A survey," *Automatica*, vol. 50, no. 6, pp. 1539–1564, 2014.

- [10] P. T. Krein, J. Bentsman, R. M. Bass, and B. C. Lesieutre, "On the use of averaging for the analysis of power electronic systems," in *Proc. IEEE Power Electron. Spec. Conf.*, Jun. 1989, pp. 463–467.
- [11] S. R. Sanders, J. M. Noworolski, X. Z. Liu, and G. C. Verghese, "Generalized averaging method for power conversion circuits," *IEEE Trans. Power Electron.*, vol. 6, no. 2, pp. 251–259, Apr. 1991.
- [12] J. W. Kimball and P. T. Krein, "Singular perturbation theory for dc-dc converters and application to PFC converters," *IEEE Trans. Power Electron.*, vol. 23, no. 6, pp. 2970–2981, Nov. 2008.
- [13] B. Lehman and R. M. Bass, "Switching frequency dependent averaged models for PWM dc-dc converters," *IEEE Trans. Power Electron.*, vol. 11, no. 1, pp. 89–98, Jan. 1996.
- [14] V. A. Caliskan, O. Verghese, and A. M. Stankovic, "Multifrequency averaging of dc-dc converters," *IEEE Trans. Power Electron.*, vol. 14, no. 1, pp. 124–133, Jan. 1999.
- [15] A. Davoudi, J. Jatskevich, and T. De Rybel, "Numerical state-space average-value modeling of PWM DC-DC converters operating in DCM and CCM," *IEEE Trans. Power Electron.*, vol. 21, no. 4, pp. 1003–1012, Jul. 2006.
- [16] C. A. Hernandez-Aramburo, T. C. Green, and N. Mugniot, "Fuel consumption minimization of a microgrid," *IEEE Trans. Ind. Appl.*, vol. 41, no. 3, pp. 673–681, May 2005.
- [17] N. Pogaku, M. Prodanovic, and T. C. Green, "Modeling, analysis and testing of autonomous operation of an inverter-based microgrid," *IEEE Trans. Power Electron.*, vol. 22, no. 2, pp. 613–625, Mar. 2007.
- [18] F. Dörfler, J. W. Simpson-Porco, and F. Bullo. (2014). "Breaking the hierarchy: Distributed control & economic optimality in microgrids," *IEEE Trans. Control Network Syst.*, 2014, to be published.
- [19] A. Bidram and A. Davoudi, "Hierarchical structure of microgrids control system," *IEEE Trans. Smart Grid*, vol. 3, no. 4, pp. 1963–1976, Dec. 2012.
- [20] Q.-C. Zhong, "Robust droop controller for accurate proportional load sharing among inverters operated in parallel," *IEEE Trans. Ind. Electron.*, vol. 60, no. 4, pp. 1281–1290, Apr. 2013.
- [21] B. B. Johnson, S. V. Dhople, A. O. Hamadeh, and P. T. Krein, "Synchronization of nonlinear oscillators in an LTI electrical power network," *IEEE Trans. Circuits Syst. I, Reg. Papers*, vol. 61, no. 3, pp. 834–844, Mar. 2014.
- [22] B. B. Johnson, S. V. Dhople, J. L. Cale, A. O. Hamadeh, and P. T. Krein, "Oscillator-based inverter control for islanded three-phase microgrids," *IEEE J. Photovoltaics*, vol. 4, no. 1, pp. 387–395, Jan. 2014.
- [23] S. H. Strogatz, *Nonlinear Dynamics and Chaos: With Applications to Physics, Biology, Chemistry, and Engineering* (ser. Studies in Nonlinearity). Boulder, CO, USA: Westview, Jan. 2001.
- [24] P. T. Krein, *Elements of Power Electronics*. New York, NY, USA: Oxford Univ. Press, 1998.
- [25] P. Jakobsen, "Introduction to the method of multiple scales," (2014). [Available]. <http://arxiv.org/pdf/1312.3651v2.pdf>
- [26] J. Rocabert, A. Luna, F. Blaabjerg, and P. Rodríguez, "Control of power converters in ac microgrids," *IEEE Trans. Power Electron.*, vol. 27, no. 11, pp. 4734–4749, Nov. 2012.
- [27] Q.-C. Zhong and Y. Zeng, "Parallel operation of inverters with different types of output impedance," in *Proc. Ind. Electron. Soc. Conf.*, Nov. 2013, pp. 1398–1403.
- [28] M. Sinha, S. Dhople, B. Johnson, N. Ainsworth, and F. Dörfler, "Nonlinear supersets to droop control," in *Proc. IEEE 16th Workshop Control Model. Power Electron.*, Jul. 2015, pp. 1–6.
- [29] Y.-R. Mohamed and E. El-Saadany, "Adaptive decentralized droop controller to preserve power sharing stability of paralleled inverters in distributed generation microgrids," *IEEE Trans. Power Electron.*, vol. 23, no. 6, pp. 2806–2816, Nov. 2008.
- [30] A. Micallef, M. Apap, C. Spiteri-Staines, J. M. Guerrero, and J. C. Vasquez, "Reactive power sharing and voltage harmonic distortion compensation of droop controlled single phase islanded microgrids," *IEEE Trans. Smart Grid*, vol. 5, no. 3, pp. 1149–1158, May 2014.
- [31] H. Avelar, W. Parreira, J. Vieira, L. de Freitas, and E. Alves Coelho, "A state equation model of a single-phase grid-connected inverter using a droop control scheme with extra phase shift control action," *IEEE Trans. Ind. Electron.*, vol. 59, no. 3, pp. 1527–1537, Mar. 2012.
- [32] N. R. Draper and H. Smith, *Applied Regression Analysis* 2nd ed. New York, NY, USA: Wiley, 1981.
- [33] F. Wang, J. Duarte, and M. Hendrix, "Active and reactive power control schemes for distributed generation systems under voltage dips," in *Proc. IEEE Energy Convers. Congr. Expo.*, Sep. 2009, pp. 3564–3571.
- [34] F. Z. Peng and J.-S. Lai, "Generalized instantaneous reactive power theory for three-phase power systems," *IEEE Trans. Instrum. Meas.*, vol. 45, no. 1, pp. 293–297, Feb. 1996.



**Brian B. Johnson** (S'08–M'13) received the B.S. degree in physics from Texas State University, San Marcos, TX, USA, in 2008, and the M.S. and Ph.D. degrees in electrical and computer engineering from the University of Illinois at Urbana-Champaign, Urbana, IL, USA, in 2010 and 2013, respectively.

He is currently an Electrical Engineer at the National Renewable Energy Laboratory, Golden, CO, USA. He received a National Science Foundation Graduate Research Fellowship in 2010. His research interests include renewable energy systems, power

electronics, and control systems.



**Mohit Sinha** received the bachelor's degree in electrical engineering from the Indian Institute of Technology, Delhi, India, in 2011. He is currently working toward the Ph.D. degree in electrical engineering from the University of Minnesota, Twin Cities, MN, USA.

He received an Electrical Engineering Department Fellowship in 2013. His research interests include modeling, analysis, and control of power-electronic systems for increasing renewable integration.



**Nathan G. Ainsworth** (S'08–M'14) received the B.S. degree in computer engineering from Purdue University, West Lafayette, IN, USA, in 2005, the M.S. and Ph.D. degrees in electrical engineering from the Georgia Institute of Technology, Atlanta, GA, USA, in 2010 and 2014, respectively, with focus in power system dynamics and distributed control theory.

From 2006 to 2008, he developed embedded control software for military power system products at DRS Test and Energy Management, LLC in Huntsville, AL, USA. He is currently a Staff Researcher at the Power Systems Engineering Center, National Renewable Energy Laboratory, Golden, CO, USA. His research interests include power system dynamics and stability, power electronics, distributed and decentralized control, and renewable generation.



**Florian Dörfler** (S'09–M'13) received the Diploma degree in engineering cybernetics from the University of Stuttgart, Stuttgart, Germany, in 2008, and the Ph.D. degree in mechanical engineering from the University of California, Santa Barbara, CA, USA, in 2013.

From 2013 to 2014, he was an Assistant Professor with the University of California, Los Angeles, CA, USA. He is currently an Assistant Professor at the Automatic Control Laboratory, ETH Zürich, Zürich, Switzerland. His primary research interests include

distributed control, complex networks, and cyberphysical systems currently with applications in energy systems and smart grids.

Dr. Dörfler received the 2009 Regents Special International Fellowship, the 2011 Peter J. Frenkel Foundation Fellowship, the 2010 ACC Student Best Paper Award, the 2011 O. Hugo Schuck Best Paper Award, the 2012–2014 Automatica Best Paper Award, and the 2015 UCSB ME Best Ph.D. thesis award. As a Coadvisor and a coauthor, he has been a finalist for the ECC 2013 Best Student Paper Award.



**Sairaj V. Dhople** (S'09–M'13) received the B.S., M.S., and Ph.D. degrees in electrical engineering from the University of Illinois, Urbana-Champaign, IL, USA, in 2007, 2009, and 2012, respectively.

He is currently an Assistant Professor at the Department of Electrical and Computer Engineering, University of Minnesota, Minneapolis, MN, USA, where he is affiliated with the Power and Energy Systems Research Group. His research interests include modeling, analysis, and control of power electronics and power systems with a focus on renewable

integration.

Dr. Dhople received the NSF CAREER Award in 2015. He currently serves as an Associate Editor for the IEEE TRANSACTIONS ON ENERGY CONVERSION.